COMMUNICATION

Check for updates

Enhancing the electronic dimensionality of hybrid organic–inorganic frameworks by hydrogen bonded molecular cations†

Fedwa El-Mellouhi, [ID] *[a] Mohamed E. Madjet, [ID][a] Golibjon R. Berdiyorov, [ID][a] El Tayeb Bentria,[a] Sergey N. Rashkeev, [ID][a] Sabre Kais, [ID][b] Akinlolu Akande, [ID][c] Carlo Motta, [ID][d] Stefano Sanvito [ID][d] and Fahhad H. Alharbi [ID][ae]

Transition-metal oxides with pyroxene structure, such as alkali-metal metavanadates, are known for their good chemical stability and have been used accordingly in many applications. In this work, we explore the possibility of enhancing the carrier transport and optoelectronic properties of hybrid inorganic–organic metavanadates MVO$_3$ by introducing molecular cations. The hydrogen bonded molecular cations are found to enhance the electronic effective dimensionality of the system. This is related to the connectivity of the atomic orbitals to form new electron and hole transport channels. For the materials considered here, these channels are formed by hydrogen bonding that, besides enhancing the stability, results in enhanced macroscopic electronic transport and enhanced photo-generated carriers relaxation time. Our study indicates that the electronic dimensionality of the hybrid metavanadates could exceed their subnanometer structural dimensionality which is a desirable feature for improving their optoelectronic properties. This concept can be generalized to a wider class of hybrid organic–inorganic frameworks.

Conceptual insights

We demonstrate a new concept enabling the enhancement of carrier transport and optoelectronic properties of transition metal oxides by incorporating hydrogen bonded molecular cations. By means of a coherent and complementary state-of-the-art computational investigation supported by comparison to experimental findings, we demonstrate that cations forming hydrogen bonds with the inorganic framework can enhance the electronic dimensionality of the system related to the connectivity of the atomic orbitals by forming new inter-channels electron and hole transport pathways. The present concept goes beyond the standard belief that the dimensionality of charge carrier transport is lower or equal to the structural dimensionality (*Mater. Horiz.*, 2017, **4**, 206–216). We demonstrate that for hydrogen bonded hybrid materials the electronic dimensionality can exceed their structural dimensionality. As a result, the extraction of the photo-generated carriers is enhanced remarkably. The concept could be generalized to the broader class of low dimensional Hybrid materials. For example, there are already strong indications that the long molecular binders used to synthesize 2D/3D, 2D and 1D lead halide perovskites might play the role of carrier transport channels; this was highlighted broadly without proof in a recent paper: *J. Am. Chem. Soc.*, 2018, **140**(23), 7313–7323.

Hybrid framework materials development is a very fast growing field in materials science because of its vast materials' space and the fact that many compounds exhibit several technologically relevant properties. One important group of hybrid materials is hybrid-halide perovskites with the composition ABX$_3$, where A = K$^+$, Rb$^+$, Cs$^+$, MA$^+$ (methylammonium), FA$^+$ (formamidinium); B = Sn^{2+}, Pb^{2+}; and X = I$^-$, Br$^-$, Cl$^-$. They recently attracted a great deal of interest because CH$_3$NH$_3$PbI$_3$ (MAPI) and HC(NH$_2$)$_2$PbI$_3$ (FAPI) show great performance in solar cell applications and may be synthesized by straightforward chemical processing methods.[1–4] The solar conversion efficiency of single-junction

hybrid-halide perovskite devices exceeds 23.3%,[1] a result probably related to a unique combination of large absorption coefficients and long carrier diffusion lengths resulting in low recombination rates.[5,6]

However, it is well known that three dimensional (3D) CH$_3$NH$_3$PbI$_3$ is structurally unstable and decomposes when exposed to moisture, oxygen, and UV light.[7,8] Therefore, the search of more stable and non-toxic materials for solar cell and optoelectronic applications that exhibit high optical absorption, good charge carrier transport, and low recombination rate is still a highly active field.

Vanadium-based oxide compounds have attracted a lot of interest in the past few decades due to their good electronic and optical properties and their thermal stability. They have already shown a great potential for practical applications as active electronic, optoelectronic, and catalytic materials.[9] Solar-light-driven water oxidation is one of the areas where vanadates have

^{a} *Qatar Environment and Energy Research Institute, Hamad bin Khalifa University, P. O. Box 34110, Doha, Qatar. E-mail: felmellouhi@hbku.edu.qa*

^{b} *Department of Chemistry, Physics, and Birck Nanotechnology Center, Purdue University, West Lafayette, Indiana 47907, USA*

^{c} *Department of Sciences, Institute of Technology, Ash Lane, Sligo, Ireland*

^{d} *School of Physics, AMBER and CRANN Institute, Trinity College, Dublin 2, Ireland*

^{e} *College of Science and Engineering, Hamad Bin Khalifa University, Doha, Qatar*

† Electronic supplementary information (ESI) available. See DOI: 10.1039/c8mh01436a

already shown a great potential due to their suitable band gaps and a convenient band edge alignment with respect to water redox levels.[10–12] Vanadates are also considered as promising electrode materials in energy storage applications for large-scale high-performance metal-ion based batteries.[13–19] This is due to several advantages of these materials: they are cheap and safe, easy to fabricate, having good thermal and environmental stability, and capability of providing high energy density. The self-activated and rare earth vanadates have also a promising potential for different lighting applications.[20,21]

Among the rich family of vanadate phosphors, metavanadate structures MVO_3 ($M = K^+$, Rb^+, and Cs^+) are considered to be good candidates for the fabrication of light emitting devices with good light rendering properties and high quantum efficiency.[22–24] Metavanadates can also be used as absorbing materials for solar cells applications[25–28] due to their earth-abundant composition, easy fabrication, non-toxicity and, most importantly, exceptional chemical and thermal stability. More-over, the strong Coulomb interactions in some of the metavanadates with Mott insulator behavior[28] triggers multiple excitons generation per incident photon, which in turn increases their quantum efficiency.[29,30] Importantly, the optoelectronic properties of metavanadates can also be refined by isovalent doping of the M-site elements.[31–33] However, a full exploitation of vanadates' potentials require a fundamental understanding of their structural and optoelectronic properties. Additionally, their transport properties require special attention, because of carrier trapping phenomenon and polaron formation processes.[28]

Using computer simulations we recently screened a set of hybrid corner-sharing metavanadates MVO_3, demonstrating the possibility of reducing their optical band gap and, hence, boosting their optical absorption properties in the visible range of the solar spectrum.[34] These materials are featured by one dimensional (1D) chains of connected $(V^{5+}O_3^{2-})^-$ tetrahedra separated by the M cations, suggesting the presence of 1D channel for carrier transport. Their crystalline structure is of a broad class of hybrid inorganic–organic frameworks in which multi-dentate organic molecules bind to multi-coordinated metal complexes (in this case, to the VO_4 networks). Hence, their subsequent application as light harvesting materials suggests the need for additional investigation of the carrier transport, mobility estimation and cooling of hot photo-generated carriers.

The concept of electronic dimensionality was recently reported[35] for describing the connectivity of the atomic orbitals in the lower conduction band (CB) and the upper valence band (VB) due to the connection of the corresponding atomic orbitals in metal-halide perovskites. It was concluded that high electronic dimensionality is more desirable than the subnanometer structural one for achieving high photovoltaic performance. It was shown that as the structural dimensionality of the prototypical Cs lead-iodine perovskite materials reduces from 3D to 2D to 1D and 0D, there is an increase in the anisotropy of the optical absorption coefficient. At the same time the charge carrier transport is reduced as the charges get confined in lower dimensions. This demonstrates a strong correlation between the structural and the electronic dimensionally. Furthermore, lead-free compounds that appear

to have a 3D structural dimensionality at the subnanometer scale, such as prototype double perovskites $Cs_2AgBiBr_6$ suffer from a reduced 0D dimensionality of electronic transport caused by the lack of overlap between the Ag and Bi states at the relevant edge of the VB.

The interplay between the structural and electronic dimensionality is nowadays being exploited as a design strategy to overcome the stability and toxicity challenges in perovskite solar cells.[35] Recently, the quest for stable lead halide perovskites resulted in lowering the 3D subnanometer dimensionality requirement in favour of 2D–3D perovskites materials.[36] Despite their reduced power conversion efficiency (PCE), 2D–3D perovskites are now considered as promising candidates for the deployment of stable hybrid perovskite in the photovoltaic market. Similarly, the limited number of non-toxic, earth abundant metal ions to design materials for solar applications is urging the community to start the exploration of materials beyond the 3D structural subnanometer dimensionality.[37]

In this work, we report the possibility of enhancing the electronic dimensionality and the photo-generated carrier life-times of hybrid inorganic–organic metavanadates by introducing organic cations into the inorganic framework. Nonetheless, the proposed technique is general and is applicable to a wide range of hybrid materials. Inorganic MVO_3 pyroxenes metavanadates usually display 1D chain connectivity, anisotropic absorption features and 1D chain anisotropic carrier transport.[34] Here we compare the charge transport properties of materials MVO_3 (where $M = Cs^+$, NH_4^+, and H_3S^+) by using density functional theory combined with a nonequilibrium Green's functions approach (DFT+NEGF) to charge transport. In addition, we have gone beyond the constant relaxation time approximation in using the Boltzmann theory of transport by calculating explicitly the carrier mobility and relaxation time (scattering time). This was achieved by taking fully into account various scattering mechanisms such as the impurity and electron–phonon scatterings. Furthermore, we have explored the impact of the electron–phonon interaction on the hot charge carrier cooling after photoexcitation using nonadiabatic molecular dynamics simulations in combi-nation with time-domain DFT. All computational details can be found in the ESI.†

We found that molecular cations can be used to change the electronic dimensionality of the system by forming extra trans-port channels related to the formation of hydrogen bonds between the hydrogenated molecular cation M^+ and the VO_4 network. The formation of these channels increases the electronic dimensionality of the material at the inter-atomic level or so-called subnanoscale and results in enhanced electronic transport properties. Our findings indicate the possibility of improving carrier transport properties of hybrid materials by suitable cation replacement for practical applications.

A. Structural and electronic properties

Fig. 1 shows the optimized structures of the pyroxene metavanadates MVO_3, featuring 1D chains of VO_4 tetrahedra linked by two
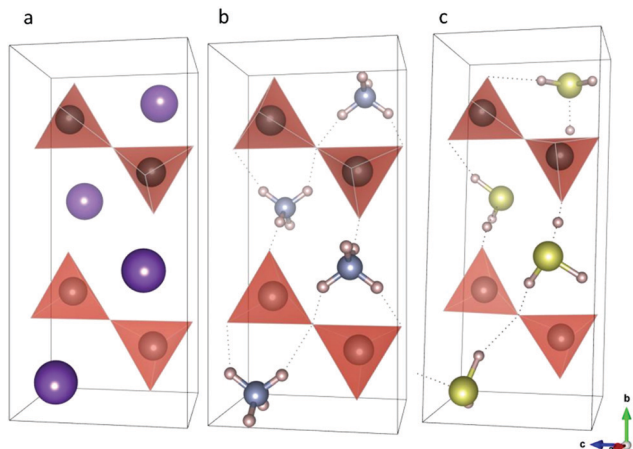
Fig. 1 Metavanadate pyroxene optimized crystal structures for: (a) CsVO$_3$, (b) NH$_4$VO$_3$, and (c) H$_3$SVO$_3$. Red: VO$_4$ polyhedra centred at V, purple: Cs, pink: H, blue: N, yellow: S. N–H$\cdots$O and S–H$\cdots$O hydrogen bond networks are presented by dotted lines.

corner oxygen atoms. The chains extend parallel to the c axis, and are separated by the cations M = Cs$^+$, NH$_4^+$, and H$_3$S$^+$, having effective ionic radii of 174, 144 and 200 pm respectively. The hybrid metavanadates with M = NH$_4^+$, H$_3$S$^+$ are characterised by the presence of N–H$\cdots$O and S–H$\cdots$O hydrogen bond networks[38] within the ab plane, as demonstrated in our earlier study.[34] The calculations started from the experimental structures[39] reported for the CsVO$_3$ and NH$_4$VO$_3$ followed by a full optimization of both atomic positions and lattice parameters. We find that the fully inorganic system CsVO$_3$ (see Fig. 1(a)) has lattice parameters a = 5.46 Å, b = 12.42 Å and c = 5.86 Å, values that are in agreement with the experimental results[39] (a = 5.39 Å, b = 12.25 Å and c = 5.78 Å). Our relaxed structure for NH$_4$VO$_3$ is also orthorhombic (Fig. 1(b)), with lattice parameters a = 4.88 Å, b = 11.99 Å and c = 5.91 Å which are also comparable to experimental parameters[39] (a = 4.91 Å, b = 11.78 Å and c = 5.83 Å). It is noticeable, as reported earlier,[34] that the VO$_4$ inter-chain distances within the ab plane are significantly reduced because of the smaller ionic radius of NH$_4^+$ compared to Cs$^+$, in addition to the presence of the bridging N–H$\cdots$O hydrogen bond network. The impact of this structural modification and hydrogen bond network on the optoelectronic and charge carrier mobility will be discussed in the following sections.

In the case of the computationally designed hybrid metavanadate[34] H$_3$SVO$_3$, the VO$_4$ inter-chain distance along the b axis chain becomes larger than in the case of CsVO$_3$ (a = 5.25 Å, b = 13.60 Å and c = 5.88 Å) while the inter-chain distance is reduced along the a axis. This is partially due to the larger ionic radius of H$_3$S$^+$ compared to Cs$^+$ but also to its dipole moment of 1.83 Debye and the directionality of the S–H$\cdots$O hydrogen bond network. Consequences on the electronic transport and carrier mobility will be discussed further in the next section.

The optical properties of the metavanadates have been discussed extensively in our previous work.[34] Overall, the optical spectra of the systems with organic cations show peak intensity comparable to the inorganic CsVO$_3$ (see Fig. S4, ESI†). However, the H$_3$SVO$_3$ sample with hydrogen bonds between cations and the inorganic framework

absorbs over a wider range of the solar spectrum due the bandgap reduction towards the visible sector. Interested readers might find further details in the ESI† and ref. 34.

In order to visualize the contribution of the M-site cations to the electronic density of states (DOS), we have calculated the band structure and orbital projected density of states (PDOS) for all considered systems. For both MVO$_3$ systems where M = Cs$^+$ and NH$_4^+$ [see Fig. S5 and S6 in the ESI†], the DOS of the system is mostly dominated by the p-states of the O atoms and the d-states of V atoms, with minor contribution from the M cation. The valence band edge (VBE) states that are relevant for carrier transport, are dominated by O, while the V dominates the CB edge, where strong hybridization of the p-states of O and d-states of V is observed. No significant contribution of the M-site elements is observed for the considered energy range. A comparison between the band structure of materials with M = Cs$^+$ and NH$_4^+$ indicates that both have bandgaps of $\sim$3 eV and their bands are degenerated at the VB and CB edges. These bands are more dispersive for NH$_4^+$ suggesting improved carrier effective masses (see Table S1, ESI†). Interestingly, the situation changes considerably in the case of H$_3$SVO$_3$. This compound has a band gap of 1.7 eV with the VB maximum (VBM) resulting from the hybridization of the p-states of O and those of S[34] (see Fig. S7, ESI†), whereas the CB minimum (CBM) remains dominated by the p-states of O and the d-states of V. This indicates significant spatial separation of possible photogenerated electron–hole pairs in the system, which may affect the lifetime of the charge carriers. Because of the appearance of these new hybridized S and O states at the VBM, the band gap of H$_3$SVO$_3$ reduces considerably as compared to the other compounds. In addition, the bands at the VB and CB edges are non-degenerate and less dispersed.

Note that spin–orbit coupling has a negligible effect on the electronic properties of the systems considered as was shown in our previous work.[34] In addition, higher level of theory such as HSE06 and G0W0 were taken into account in the same work to correct the PBE-DFT bandgap underestimation issue.[34] The increased interchain distance along the b direction combined with the non-negligible distortion of the VO$_4$ tetrahedra and the crystal field splitting are responsible for lifting the bands degeneracy. This attempts to reduce the band gap of metavanadates to the visible region by cation exchange, while successful in the case of M = H$_3$S$^+$, appears to affect considerably the curvature of the bands and consequently the carrier effective masses. Nevertheless, under finite temperature operating conditions, an efficient collection of photogenerated charge carriers requires: (a) good electrical conductivity; (b) a long carrier scattering time or so-called relaxation time, and; (c) a long timescale of photoexcited carrier relaxation to the band edges to ensure their collection and delay the radiative/non-radiative recombination.

B. Microscopic electronic transport properties

In this section, we study the electronic transport properties of the materials under consideration by using the DFT+NEGF approach (details of the approach used can be found in ESI†).
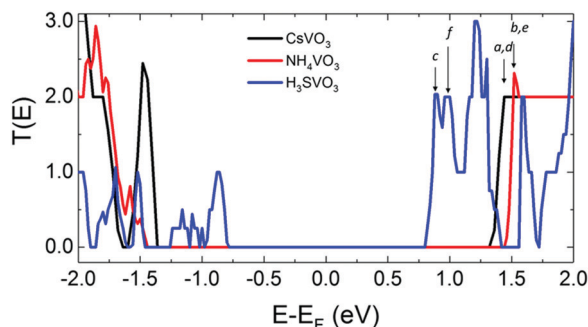
Fig. 2 (top) Calculated zero bias transmission coefficients along the VO_4 chains (parallel to c axis) as a function of electron energy for $CsVO_3$, NH_4VO_3, and H_3SVO_3 samples. Arrows and labels (a–f) point to relevant electron transmission channels at CBM and CBM + 1. The zero of energy is set to be the Fermi level of the given system.

We start by analysing the zero bias transmission spectra, $T(E)$, which are shown in Fig. 2 as a function of the electronic energy for all the considered samples. The transmission is calculated along the VO_4 chains (parallel to c axis, see Fig. S2, ESI†) while the energy zero is set to be the Fermi level of the system. The transmission at the CB edge (CBE) for $CsVO_3$ and NH_4VO_3 is characterized by a broad and doubly degenerate peaks [arrows (a and d)], with a transmission amplitude around $T = 2.0$. This indicates that both channels along the VO_4 chains are activated simultaneously and become available for electronic transport. Interestingly, NH_4VO_3 exhibits a slight increase at the CB state transmission as labelled by the arrows (b and e) giving indication that additional electron transmission channels might become available. Interestingly, the transmission at CBE for H_3SVO_3 is characterized by two distinct non-degenerate peaks shaved at an amplitude of 2.0 as indicated by the arrows c and f. The lifted degeneracy in the transmission might originate from the lifted degeneracy observed earlier in the electronic band structure. It indicates that each VO_4 chains channel might be activated separately in addition to existing channels of transport. The VBE transmission spectrum for $CsVO_3$ is characterized by a well pronounced peak with an amplitude exceeding 2.0, while NH_4VO_3 has a wide multi-dented peak with a maximum reaching up to an amplitude of 3.0. The VBE transmission spectrum for H_3SVO_3 is a single peak extending up to energies (VBM-0.5 eV), with an amplitude of 1.0. Worth noting that the states at the VBE are hybridized S and O p-states as shown in the previous section in the PDOS and band structure analysis. Hence, despite the lifted degeneracy observed for the H_3SVO_3 transmission spectrum, the material has the smallest zero-transmission area due to its smallest band gap. This means that upon application of a bias voltage H_3SVO_3 will be the material for which the current on-set will appear at the lowest voltage. We have calculated electrostatic potential variations, which are also one of the important factors affecting the charge transport on the system. Fig. S3 (ESI†) shows the averaged electrostatic difference potential for the considered systems along the transport direction. For both samples, we obtained periodic potential oscillations. However, both the amplitude and the frequency of the oscillations are larger in

the NH_4VO_3 sample (dashed red curve) as compared to the ones in H_3SVO_3 system (solid black curve) suggesting that the scattering of the electrons from these potential oscillations reduce their transport through the system. This being said, electrostatic potential is not the only mechanism limiting the carrier scattering time because e-phonon interaction is also important as will be discussed in the next section.

Looking more closely at the microscopic transport, it is known that localization of electronic states is one of the main factors affecting the electronic transmission. Fig. 3 shows the isosurface plots of the projected self-consistent Hamiltonian eigenstates (PSH) of all the considered materials for the peaked transmissions that correspond to the CBM (a–c) and CBM + 1 (d–f) states. In most systems, the visualized electronic transmission channels (Fig. 3a–f) extend along the two available VO_4 chain channels. Interestingly, in the case of NH_4VO_3 and H_3SVO_3 hybrid metavanadates, the PSH are spread over the molecule as well, which means that the corresponding transport channels are opened so that some electrons can pass through the interchain region perpendicular to the c axis. In fact, the electronic states become extended within the VO_4 interchain region passing by the N–H···O and S–H···O hydrogen bonds explaining the transmission values higher than 2.0 observed in Fig. 2. This is even more evident from Fig. 3c and f for every individual VO_4 channel. Additional channels across the VO_4 chains are observed by visual inspection indicating the extra
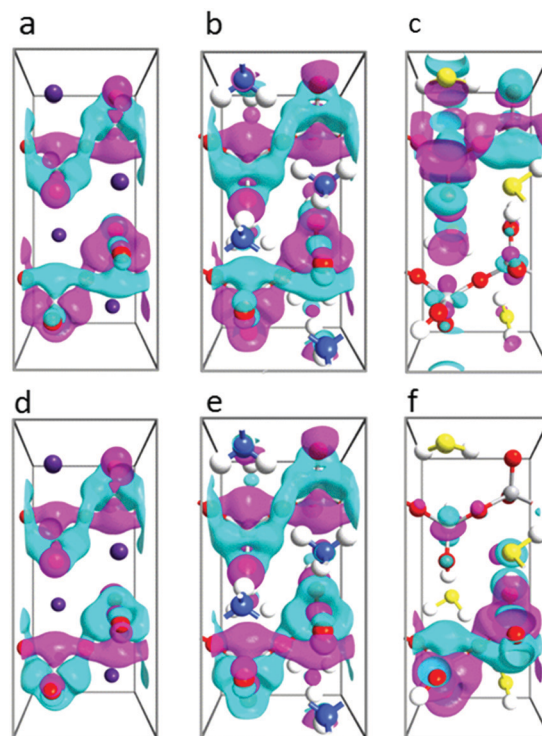

Fig. 3 Zero bias isosurface plots (isovalues are −0.05 (cyan colour) and +0.05 (magenta colour) $Å^{-3/2}$) of the projected self-consistent Hamiltonian (PHS) eigenstates for the peaked transmissions that correspond to the conduction band minimum (CBM) (a–c) and CBM + 1 (d–f) states of the samples $CsVO_3$ (a and d), NH_3VO_3 (b and e), and H_3SVO_3 (c and f).

transmission channel opening due to the extended electronic states between the VO_4 channels. Such delocalization occurs through the hydrogen bonded H_3S molecule In fact, electrons coming from one metal electrode with continuous energy interaction with electrons at molecular orbitals and then transport through the VO_4 chains to the other electrode. If molecules interacting with the VO_4 chains *via* hydrogen bonding are present, the orbital is delocalized across the molecule. Thus, an electron entering the material at the energy of the orbital has a high probability of going through the molecule to reach the neighbouring VO_4 channel and, hence, creating additional channels of transport.

We conclude that the devices made of metavanadates containing hydrogen bonds can exhibit additional transport channels than those made of materials without molecular cations since O atoms play the role of electron donors while nitrogen and sulfur atoms are electron acceptors. These additional channels of transport might serve to spatially separate the e–h pair and help avoiding the rapid exciton recombination. The investigation done here indicates that the electronic dimensionality of the hybrid metavanadates might exceed their subnanometer structural dimensionality, which is a desirable feature for enhancing compounds' optoelectronic properties.[35]

C. Macroscopic charge carrier mobility and scattering time

In order to further elucidate the increased electronic dimensionality observed in the hybrid organic–inorganic metavanadates, we estimated the direction-dependent electrical conductivity of the three samples by solving the Boltzmann transport equations (BTEs). Computational details can be found in the ESI.† At finite temperature device operating temperature, the macroscopic charge transport depends not only on the electrical conductivity of these materials but also on the carrier scattering mechanisms such as interactions with phonons, inelastic scattering mechanisms, ionized impurities, piezoelectricity, deformation potential and charged dislocations. These scattering mechanisms can be summated using Matthiessen's rule for the elastic scattering and the Fermi golden rule for phonon scattering to calculate the carrier relaxation time (τ_s).[41] Although, it is common to employ the constant relaxation time approximation (BTE-CRA) for a wide class of thermoelectric materials,[40,41] our initial assessment demonstrated that this approach is not valid for the pyroxene metavanadates. This is because of the large differences in the calculated polar optical phonon (PO) frequencies between $CsVO_3$ and NH_4VO_3 (see Table S1, ESI†) raising the need to explicitly compute τ_s. Hence, we calculate the k-dependent relaxation time, which is combined with the electrical conductivity σ/τ_s obtained from solving BTE and used to estimate the electron and hole mobility $\mu = \sigma/(ne)$, where n is charge carrier concentration (in cm^{-3}) and e is the electron charge.

An attempt was made before to calculate transport, using "*ab initio* Model for mobility calculation using Boltzmann Transport equation" – the so called aMoBT model[42] which fully captures the elastic and inelastic scattering of charge carriers using a single band model. Despite our highly accurate calculation of band structure, deformation potential, dielectric function, and optical phonon frequency (see Table S1, ESI†), this approach did not capture accurately the electron–phonon scattering that is dominant at high temperatures. This is due to inappropriateness of the single band model to our metavanadates exhibiting band structure with multiple band degeneracy and band crossing (see Fig. S5–S7, ESI†). Nevertheless, it helped us confirm that scattering mechanism such as ionized impurity do not dominate the carrier scattering and could be neglected, strengthening the assumption that electron–phonon scattering is the most dominant mechanism.

The newly released BoltzTraP2[43] software package, besides its enhanced electronic band fitting performance over Boltztrap,[44] calculates a smoothed Fourier expression of periodic functions and the Onsager transport coefficients using the linearized BTE. It uses as input only the bands and k-dependent phonon energies, as well as the intra-band optical matrix elements and scattering rates (if available).[43] The scattering rate was computed by means of Abinit package,[45] with its robust implementation of electron–phonon interaction within density functional perturbation theory (DFPT).[46]

The electron phonon scattering has been fully accounted for by fulfilling the conservation of energy and $k' - k = q + g$ with g a reciprocal lattice vector k, q are the grid of points in the BZ. The feature to calculate relaxation time for semiconductor case was implemented in anaddb routine (part of the Abinit package) only in 2016 and it requires large computational power.[46] Calculation details are presented in the ESI.†

The resulting calculated relaxation times from BoltzTraP2[43] are in the femtosecond range, namely, τ_s = 3.9 fs for $CsVO_3$, 85 fs for NH_4VO_3, and 20 fs for H_3SVO_3. The order of magnitude for τ_s is comparable with the values reported earlier for efficient photoabsorbers such as MAPI[47] (τ_s = 10 fs) and $CuSnSbS_3$[41] (τ_s = 40 fs). These calculated values provide a better representation of the thermoelectric properties, and give a strong indication of transport properties for this class of materials.

Fig. 4 presents the hole and electron mobility μ (in $cm^2\ V^{-1}\ s^{-1}$) at 300 K averaged over all crystallographic directions for $CsVO_3$, NH_4VO_3, and H_3SVO_3 as a function of the charge concentration ρ. The electron mobility averaged over all transport directions of transport for the inorganic $CsVO_3$ reaches a maximum
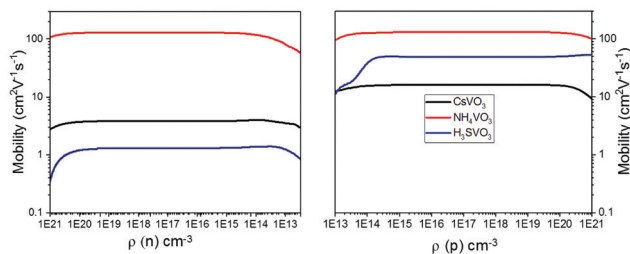

Fig. 4 Average hole and electron mobility μ in ($cm^2\ V^{-1}\ s^{-1}$) for $CsVO_3$ (black), NH_4VO_3 (red) and H_3SVO_3 (blue) as a function of the charge concentration, ρ, calculated with k-dependent relaxation time.

$\mu = 16.5$ cm^2 V^{-1} s^{-1} due to its small relaxation time. Interestingly, NH$_4$VO$_3$ has an order of magnitude higher mobility $\mu = 130$ cm^2 V^{-1} s^{-1} while H$_3$SVO$_3$ has an intermediate value of $\mu = 50$ cm^2 V^{-1} s^{-1}. The hole mobility for the inorganic CsVO$_3$ reaches a maximum of $\mu = 4.0$ cm^2 V^{-1} s^{-1}, NH$_4$VO$_3$ has a two orders of magnitude higher mobility of $\mu = 130$ cm^2 V^{-1} s^{-1} while H$_3$SVO$_3$ had the lowest hole mobility, $\mu = 1.3$ cm^2 V^{-1} s^{-1}. It is impressive that hybrid metavanadate, NH$_4$VO$_3$ has comparable average electron and hole mobilities, an advantageous feature for the generation of current and charge extraction.

Comparing again the crystallographic and electronic dimensionalities, one notices from Fig. 5 and Fig. S8–S12 (ESI†) that conductivity and mobility of metavanadates as function of the charge concentration are anisotropic in all three directions xx, yy and zz. However, interesting electronic dimensionally features emerge for each of the considered material: CsVO$_3$ has a high electron mobility along the zz direction (parallel to the VO$_4$ chains) reaching up to 106 cm^2 V^{-1} s^{-1} and insignificant mobility along the directions perpendicular to the chains namely xx and yy (see Fig. S9, ESI†). In contrast, it has low hole mobility along all crystallographic directions, a fact that can be attributed to the single flat band lying at close to the VB, and the small conductivity peak is observed in Fig. S8 (ESI†). This dominates for carrier concentration less than 3×10^{22} cm^{-1}. Hence, CsVO$_3$ has both a 1D structural and electronic dimensionality.

The direction-dependant conductivity and mobility for NH$_4$VO$_3$ are shown in Fig. 5. The electron mobility here is also dominated by the zz component. However, a noticeable increase by an order of magnitude in the mobility along yy is clearly seen from the insets of Fig. S10 (ESI†). Moving to the hole mobilities, a significant enhancement in the mobility along the xx direction dominates the hole transport where the zz direction motilities start to raise only at carrier concentration higher than 3×10^{22} cm^{-1}. The direction dependent conductivity and mobility assessment of NH$_4$VO$_3$ confirms our earlier finding using DFT+NEGF about the opening of additional electronic channels of transport along the xx and yy directions in the interchain region which are absent in the case of the inorganic metavanadate pyroxene CsVO$_3$. It also confirms the earlier claim about the activation of channels along the N–H···O hydrogen bonds as additional channel of transport, contributing to enhancing the electronic dimensionality above 1D. Interestingly, NH$_4$VO$_3$ offers an interesting anisotropic scenario of long lived electron–hole pair

due to the spatial separation after photoexcitation, with electrons transporting predominantly along the VO$_4$ chains (zz direction) combined with hole transport along the xx direction.

H$_3$SVO$_3$ displays features similar to NH$_4$VO$_3$ (Fig. S11 and S12, ESI†): the electron transport is dominated by the zz component, and the activated channels of transport along xx and yy could be clearly seen as components confirming our earlier finding using DFT+NEGF. The mobility along the xx and yy directions also contributes in making the averaged electron mobility higher than that of CsVO$_3$. Here, we also witness an enhanced electronic dimensionality beyond 1D by the activation of the S–H···O hydrogen bonds as additional channel of transport between VO$_4$ chains. Unfortunately, this compound has a weak hole mobility compared to the others. This low-hole mobility can be explained by the one band contributing in the conductivity (see band structure in Fig. S7, ESI†) which is also noticeable from the modest conductivity peak in Fig. S11 (ESI†).

The temperature dependent mobility is shown in Fig. S13 (ESI†), demonstrating that both electron and hole mobility decreases with increasing temperature for all metavanadate compounds. This is an expected behaviour due to the fact that the electron–phonon scattering mechanism dominates the total relaxation time term above room temperature. Nonetheless, the compounds keep reasonably good mobilities at room temperatures that will be utilized in Section E to evaluate the carrier diffusion coefficient and the diffusion lengths. Before we present our results on these, the hot carrier lifetimes are computed and discussed, comparing two hybrid metavanadates, in the next section.

D. Photo-generated charge carrier relaxation time

In the present study, the investigation of the cooling process of hot electrons and hot holes is done separately. We consider the excitation of electrons from the VBM to states in the CB with energy ΔE_e above the CBM. Then we investigate the relaxation dynamics of hot electrons from these states to the CBE. To study the thermalization of hot holes, we promote electrons from states below the VBM with energy ΔE_h. Since the electron–hole interaction is neglected in this approach, the relaxation occurs due to the interaction between charge carriers of the same type and the interaction of the charge carriers with phonons. More details about the computational methodology can be found in the ESI.†

Fig. 6 shows the electron (top panel) and hole (bottom panel) population decay time from different initial excited state energies $\Delta E_e / \Delta E_h$ (above the CBM/below the VBM) for the three systems. It is clear that the hot carrier decay process is faster in the case of NH$_4$VO$_3$. For most of the excited state energies, the cooling process of hot-carriers in CsVO$_3$ system is faster than the one in H$_3$SVO$_3$ and slower than the one in NH$_4$VO$_3$. The increase in the hot electron relaxation time at 0.81 eV, which corresponds to CBM + 4 state as initially populated state, is mainly due to larger energy gap between CBM + 4 and CBM + 3 states. Note that this energy gap is about 0.4 eV (see also Fig. 7) for CsVO$_3$ which is
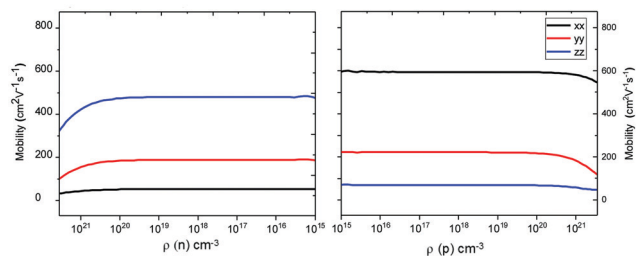

Fig. 5 Hole mobility and electron mobility tensor μ in (cm^2 V^{-1} s^{-1}) of NH$_4$VO$_3$ as a function of the charge concentration (ρ) in the three cartesian directions calculated with k-dependent relaxation time.
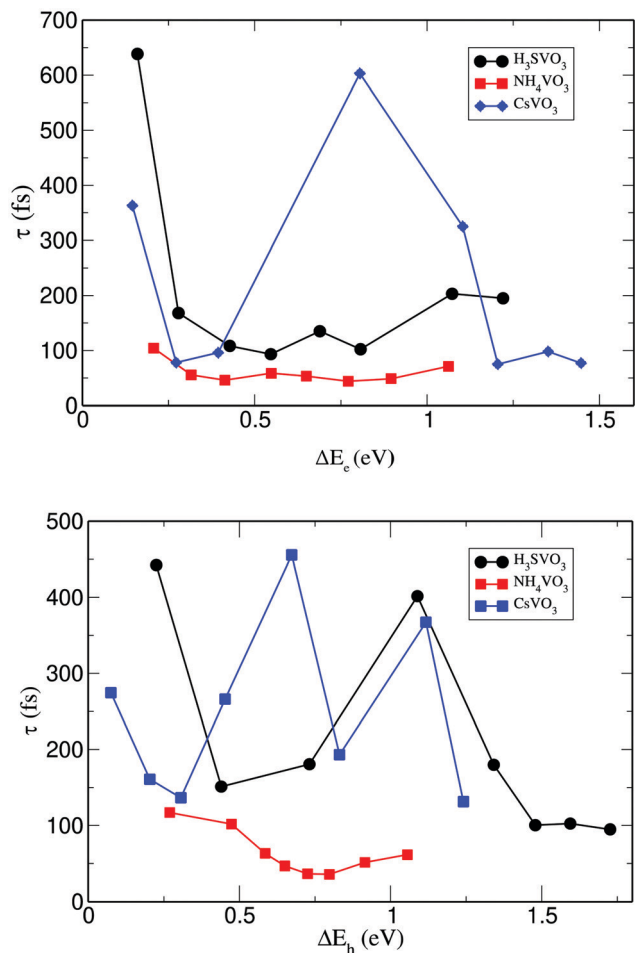
Fig. 6 Electron (top panel) and hole (bottom panel) relaxation times (fs) for $CsVO_3$, H_3SVO_3 and NH_4VO_3. Electrons are excited to states with an energy ΔE_e above the conduction band minimum and holes are excited to states deeper in the valence band with an energy ΔE_h from the valence band maximum.

Fig. 7 Nonadiabatic couplings (in meV) between states in the space of KS orbital indices for $CsVO_3$, H_3SVO_3 and NH_4VO_3. Here $j = 0$ means the VBM state.

much larger than the one for H_3SVO_3 and NH_4VO_3 systems, as can be seen in Fig. 6.

Fig. S14 (ESI†) shows the time dependence of the electronic populations of the (CBM + 4) state where the electron is initially excited, for H_3SVO_3 and NH_4VO_3 systems. For the sake of better illustration, we present the sum of the two lowest energy electron states [i.e., CBM01 = CBM + (CBM + 1)] populations as a final state population. In order to extract the population decay time, the time dependence of the initial excited state population and the final state population were fitted by a sum of exponential and Gaussian functions. Fig. S14 (ESI†) shows that the initial excitation energy, ΔE_e, is very similar for both systems. For NH_4VO_3, the initial excited state is almost completely depopulated within 200 fs, and the decay time extracted from the fitting is 58 fs, which represents an ultrafast decay process of the initial excited state. It takes about 2 times longer time for the complete transfer of the population to the final energy state (CBM01). For H_3SVO_3, the complete decay of the initially populated state (CBM + 4) takes place after 400 fs,
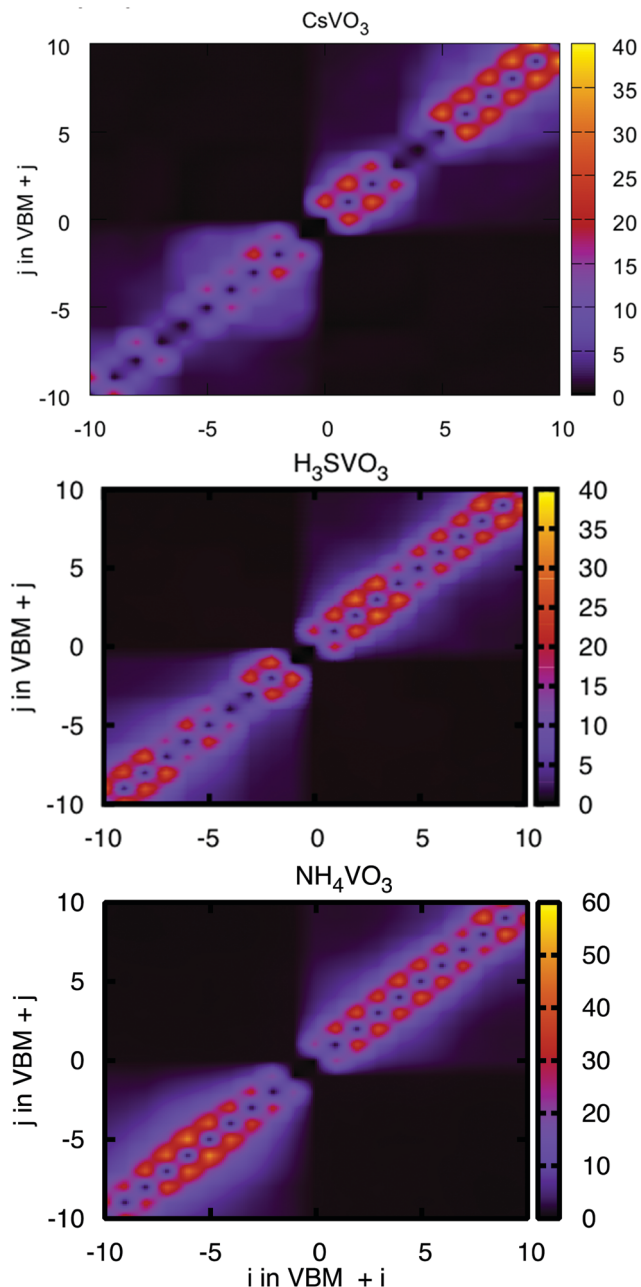
which is 2 times slower than in the case of NH_4VO_3. Also, the decay time of the (CBM + 4) state for H_3SVO_3 (93 fs) is about 2 times longer than for NH_4VO_3 (58 fs). As expected, carrier population dynamics also depends on the excitation energy as can be seen from Fig. 6 where the electron/hole relaxation time from different excited states is plotted for both systems. For all considered ΔE_e, the electron population decay for NH_4VO_3 happens always faster than for H_3SVO_3. It is evident from the Fig. 6 that except for energies $\Delta E_e < 0.25$ eV, the decay time increases slightly with increasing the excitation energy. Close to the band edge, the relaxation process of hot electrons becomes

slower. As an example, for H_3SVO_3 the decay time is more than 600 fs for $\Delta E_e \sim 0.2$ eV and it is only 100 fs at $\Delta E_e \sim 0.4$ eV. As a matter of comparison, previous calculations reported electron relaxation time of 179 fs and 679 fs for FAPI and MAPI respectively in line with the order of magnitudes reported in the present work.[48]

Fig. S15 (ESI†) shows the hole population decay after initial excitation to the excited state (VBM-2) for the considered two systems. Similar to the case of electron population decay, the hole population decay is faster in the case of NH_4VO_3 compared to H_3SVO_3. The energy of the initial excited hole state in NH_4VO_3 is a bit higher but its depopulation occurs faster than in the case of H_3SVO_3. From Fig. S15 (ESI†) it is evident that hole population decay time from VBM-2 in both systems is the same as the population decay time of VBM01 state. This is simply due to the fact that there is a direct population transfer from VBM-2 to VBM01 without involving any intermediate states. However, for hot electron relaxation from CBM + 4 in both considered systems, the population time of the lowest state CBM01 is much longer than the population decay time of the initial states as shown in Fig. 6. This is because the decay from the initial state to the lower state is involving few inter-mediate states which explains the delay of the population transfer to the lower state after depopulating the initial excited state. Interestingly, polar optical (PO) phonon frequencies responsible of the electron–phonon scattering identified in the previous section seems also to be responsible of the hot carrier cooling. Energy dependent carriers thermalization process is still visible especially for H_3SVO_3 system (see Fig. 6). Fig. S16 (ESI†) shows the phonon modes driving the hole and electron relaxations from various high energy states for H_3SVO_3 without convolution. It is clear from the plot that hole relaxation is driven only by the PO vibration mode around 85–100 cm^{-1}, while electron relaxation is driven by the PO plus a contribution from the mode at 300 cm^{-1}. Worth noting that this particular polar optical phonon mode of frequency 96 cm^{-1} mode is also responsible of the phonon-carrier scattering during their diffusion across the sample as shown in the previous section (see Table S1, ESI†).

Fig. 7 shows the nonadiabatic coupling (NAC) between states in the valence and conduction bands for all considered systems. The NAC represents the carrier–phonon interaction, which allows transition between excited states in the system and therefore drives the thermalization process of hot carriers. To our understanding such reduced thermalization process for H_3SVO_3 is related to the smaller NACs as compared to the one for NH_4VO_3 (see Fig. 7) and also to spatial separation of charge carriers in the case of H_3SVO_3 system shown earlier. Also, as a general trend, the cooling process of hot-carriers in H_3SVO_3 is slower than in $CsVO_3$. Thus, the M-site cations play an important role in the non-radiative cooling of photo-excited charge carriers. This thermalization process is driven by carrier–phonon interactions through lattice vibrations which is one of the main mechanisms of interband relaxation of hot carriers in semiconducting materials. The strength of these interactions is reflected in the NACs (Fig. 7).

E. Room temperatures carrier diffusion coefficient and diffusion length

For the practical applications of the metavanadates as photo-active absorbers, it is important to evaluate their transport properties not only under doping, but also under charge injection regime at operating temperature. After calculating the electrical mobility, scattering time as well as the hot carrier relaxation time in the previous sections, one could correlate all calculated quantities to estimate the diffusion coefficients. The diffusion coefficient is directly related to the mobility *via* Einstein's relation: $D = \mu_{ave}k_bT/e$, where $\mu_{ave} = \dfrac{n_e\mu_e + n_h\mu_h}{n_e + n_h}$ is the mobility calculated at similar carrier concentration for electrons and holes ($n_e = n_h$) at 300 K as reported in Table S2 (ESI†). In terms of average mobility, the hybrid materials NH_4VO_3 and H_3SVO_3 show average mobilities superior to those of their inorganic counterpart $CsVO_3$. Consequently, the diffusion coefficient of NH_4VO_3 is one order of magnitude higher than $CsVO_3$ while H_3SVO_3 sits in between.

Quantitatively, D increases from ~ 0.25 cm^2 s^{-1} for $CsVO_3$ to ~ 0.7 for H_3SVO_3 and reaches up to ~ 3.35 cm^2 s^{-1} for NH_4VO_3 (see Table S3, ESI†). Worth noting, for sake of comparison, that for hybrid perovskite light absorbers such as MAPI, diffusion coefficients of 1.04 cm^2 s^{-1} for holes and 1.5 cm^2 s^{-1} for electrons have been reported.

Another important quantity to evaluate the quality of carrier collection in photo absorbers could be deduced from the diffusion length $L_D = \sqrt{(D\tau_{rec})}$, that represents the average diffusion distance of the minority carriers with a specific life-time from the point of generation.[49] Diffusion lengths are closely related to the carrier collection probability and are indication of materials having longer carrier lifetimes. For comparison, MAPI has $L_D = 0.105$ μm for holes and 0.129 μm for electrons.[50] The estimation of carrier lifetime requires the evaluation of the recombination time which in the case of these indirect band gap semiconductors not straightforward. Nevertheless, we make the rough assumption that the minimum recombination time τ_{rec}^{min} is at least equal to the longest carrier cooling time extracted from the previous section, namely $\tau_{rec}^{min} = 550$ fs for H_3SVO_3 and $\tau_{rec}^{min} = 105$ fs for NH_4VO_3 and $CsVO_3$. Hence, the lower limit of the diffusion length $L_D^{min} = \sqrt{(D\tau_{rec}^{min})}$ at 300 K is reported in Table S4 (ESI†) for a range of injected carrier densities. It shows that under charge injection regime ($n_e = n_h$) at room temperature, NH_4VO_3 and H_3SVO_3 have remarkably high diffusion length ($L_D^{min} > 0.5$ μm) surpassing their inorganic counterparts demonstrating improved photogeneration and charge collections properties.

In summary, we demonstrated that enhanced electronic transport is obtained in the case of NH_4VO_3 and H_3SVO_3 due to the formation of extra transport channels, created by hydrogen bonding.

The result is mainly attributed to the formation of hydrogen bonds bridging between the VO_4 chains and the organic cation

along which electrons could be transferred thus enhancing greatly the separation and transfer efficiencies of charge and the electronic dimensionality of these materials. The present concept goes beyond the standard belief that the dimensionality of charge carrier transport is lower or equal to the subnanometer structural dimensionality.[35] Hence cation replacement can be used as an effective tool to tune the optoelectronic properties of hybrid materials. For example, there are already strong indications that the long molecular binders used to synthesize 2D/3D, 2D and 1D lead halide perovskites might play the role of carrier transport channels.[51]

We show that significant enhancement of photovoltaic properties could be achieved while using an organic M-site cation by enhancing the carrier mobility. We note also an important increase of the intra band relaxation time. This is not expected to impact the performance of conventional cells, which is controlled by the carrier lifetime but could be of interest in case novel cells enabling the collection of hot carriers.

Conclusions

We demonstrated a new concept enabling the enhancement of the charge carrier transport and optoelectronic properties of transition metal oxides by incorporating hydrogen bonded molecular cations. This was achieved by means of a coherent and complementary state-of-the-art computational investigation supported by comparison to experimental findings. We showed that cations forming hydrogen bonds with the inorganic framework can enhance the electronic dimensionality of the system related to the connectivity of the atomic orbitals of the molecular cation to the framework and forming new inter-channels electron and hole transport pathways. We demonstrated that for hydrogen bonded hybrid materials the electronic dimensionality could exceed their structural subnanometer dimensionality. This concept could be generalized to the broader family of hybrid materials.

Conflicts of interest

There are no conflicts to declare.

Acknowledgements

Notes and references

1 N.-G. Park, *MRS Bull.*, 2018, **43**, 527–533.
2 J. Burschka, N. Pellet, S.-J. Moon, R. Humphry-Baker, P. Gao, M. K. Nazeeruddin and M. Grätzel, *Nature*, 2013, **499**, 316.
3 M. Liu, M. B. Johnston and H. J. Snaith, *Nature*, 2013, **501**, 395.
4 G. E. Eperon, S. D. Stranks, C. Menelaou, M. B. Johnston, L. M. Herz and H. J. Snaith, *Energy Environ. Sci.*, 2014, **7**, 982–988.
5 H.-S. Kim, S. H. Im and N.-G. Park, *J. Phys. Chem. C*, 2014, **118**, 5615–5625.
6 R. E. Brandt, V. Stevanović, D. S. Ginley and T. Buonassisi, *MRS Commun.*, 2015, **5**, 265–275.
7 J. Berry, T. Buonassisi, D. A. Egger, G. Hodes, L. Kronik, Y. Loo, I. Lubomirsky, S. R. Marder, Y. Mastai and J. S. Miller, *Adv. Mater.*, 2015, **27**, 5102–5112.
8 Y.-Y. Zhang, S. Chen, P. Xu, H. Xiang, X.-G. Gong, A. Walsh and S.-H. Wei, *Chin. Phys. Lett.*, 2018, **35**, 36104.
9 B. M. Weckhuysen and D. E. Keller, *Catal. Today*, 2003, **78**, 25–46.
10 A. Kudo, K. Omori and H. Kato, *J. Am. Chem. Soc.*, 1999, **121**, 11459–11467.
11 M. Oshikiri, M. Boero, J. Ye, Z. Zou and G. Kido, *J. Chem. Phys.*, 2002, **117**, 7313.
12 P. Li, N. Umezawa, H. Abe and J. Ye, *J. Mater. Chem. A*, 2015, **3**, 10720–10723.
13 H. Ma, S. Zhang, W. Ji, Z. Tao and J. Chen, *J. Am. Chem. Soc.*, 2008, **130**, 5361–5367.
14 J. Chen and F. Cheng, *Acc. Chem. Res.*, 2009, **42**, 713–723.
15 Y. Shi, J.-Z. Wang, S.-L. Chou, D. Wexler, H.-J. Li, K. Ozawa, H.-K. Liu and Y.-P. Wu, *Nano Lett.*, 2013, **13**, 4715–4720.
16 G. Yang, H. Cui, G. Yang and C. Wang, *ACS Nano*, 2014, **8**, 4474–4487.
17 C. Deng, S. Zhang, Z. Dong and Y. Shang, *Nano Energy*, 2014, **4**, 49–55.
18 Q. Van Overmeere and S. Ramanathan, *Electrochim. Acta*, 2014, **150**, 83–88.
19 S. Ni, J. Ma, J. Zhang, X. Yang and L. Zhang, *J. Power Sources*, 2015, **282**, 65–69.
20 T. Nakajima, M. Isobe, T. Tsuchiya, Y. Ueda and T. Manabe, *Opt. Mater.*, 2010, **32**, 1618–1621.
21 X. Qiao, Y. Li, Y. Wan, Y. Huang, H. Cheng and H. J. Seo, *J. Alloys Compd.*, 2016, **656**, 843–848.
22 T. Nakajima, M. Isobe, T. Tsuchiya, Y. Ueda and T. Kumagai, *Nat. Mater.*, 2008, **7**, 735.
23 T. Nakajima, M. Isobe, T. Tsuchiya, Y. Ueda and T. Kumagai, *J. Lumin.*, 2009, **129**, 1598–1601.
24 T. Nakajima, M. Isobe, Y. Uzawa and T. Tsuchiya, *J. Mater. Chem. C*, 2015, **3**, 10748–10754.
25 T. Arima, Y. Tokura and J. B. Torrance, *Phys. Rev. B: Condens. Matter Mater. Phys.*, 1993, **48**, 17006.
26 T. Arima and Y. Tokura, *J. Phys. Soc. Jpn.*, 1995, **64**, 2488–2501.
27 E. Assmann, P. Blaha, R. Laskowski, K. Held, S. Okamoto and G. Sangiovanni, *Phys. Rev. Lett.*, 2013, **110**, 78701.
28 L. Wang, Y. Li, A. Bera, C. Ma, F. Jin, K. Yuan, W. Yin, A. David, W. Chen and W. Wu, *Phys. Rev. Appl.*, 2015, **3**, 64015.
29 E. Manousakis, *Phys. Rev. B: Condens. Matter Mater. Phys.*, 2010, **82**, 125109.
30 J. E. Coulter, E. Manousakis and A. Gali, *Phys. Rev. B: Condens. Matter Mater. Phys.*, 2014, **90**, 165142.
31 S. Miyasaka, T. Okuda and Y. Tokura, *Phys. Rev. Lett.*, 2000, **85**, 5388.

32 J. G. Cheng, Y. Sui, J. S. Zhou, J. B. Goodenough and W. H. Su, *Phys. Rev. Lett.*, 2008, **101**, 87205.

33 B. V. Slobodin, A. V. Ishchenko, R. F. Samigullina, O. S. Teslenko, B. V. Shul'gin and D. Y. Zhurakovskii, *Inorg. Mater.*, 2011, **47**, 1126.

34 F. El-Mellouhi, A. Akande, C. Motta, S. N. Rashkeev, G. Berdiyorov, M. E.-A. Madjet, A. Marzouk, E. T. Bentria, S. Sanvito, S. Kais and F. H. Alharbi, *ChemSusChem*, 2017, **10**(9), 1931–1942.

35 Z. Xiao, W. Meng, J. Wang, D. B. Mitzi and Y. Yan, *Mater. Horiz.*, 2017, **4**, 206–216.

36 G. Grancini, C. Roldán-Carmona, I. Zimmermann, E. Mosconi, X. Lee, D. Martineau, S. Narbey, F. Oswald, F. De Angelis and M. Graetzel, *Nat. Commun.*, 2017, **8**, 15684.

37 A. Walsh, D. O. Scanlon and S.-H. Wei, *APL Mater.*, 2018, **6**, 84401.

38 Ľ. Smrčok, B. Bitschnau and Y. Filinchuk, *Cryst. Res. Technol.*, 2009, **44**, 978–984.

39 F. C. Hawthorne and C. Calvo, *J. Solid State Chem.*, 1977, **22**, 157–170.

40 C. Motta, F. El-Mellouhi, S. Kais, N. Tabet, F. Alharbi and S. Sanvito, *Nat. Commun.*, 2015, **6**, 7026.

41 A. Faghaninia, G. Yu, U. Aydemir, M. Wood, W. Chen, G.-M. Rignanese, G. J. Snyder, G. Hautier and A. Jain, *Phys. Chem. Chem. Phys.*, 2017, **19**, 6743–6756.

42 A. Faghaninia, J. W. Ager III and C. S. Lo, *Phys. Rev. B: Condens. Matter Mater. Phys.*, 2015, **91**, 235123.

43 G. K. H. Madsen, J. Carrete and M. J. Verstraete, *Comput. Phys. Commun.*, 2018, **231**, 140–145.

44 G. K. H. Madsen and D. J. Singh, *Comput. Phys. Commun.*, 2006, **175**, 67–71.

45 X. Gonze, F. Jollet, F. A. Araujo, D. Adams, B. Amadon, T. Applencourt, C. Audouze, J.-M. Beuken, J. Bieder and A. Bokhanchuk, *Comput. Phys. Commun.*, 2016, **205**, 106–131.

46 X. Gonze, F. Jollet, F. A. Araujo, D. Adams, B. Amadon, T. Applencourt, C. Audouze, J.-M. Beuken, J. Bieder and A. Bokhanchuk, *Comput. Phys. Commun.*, 2016, **205**, 106–131.

47 C. Motta, F. El-Mellouhi and S. Sanvito, *Sci. Rep.*, 2015, **5**, 12746.

48 M. E. Madjet, A. Akimov, F. El-Mellouhi, G. Berdiyorov, S. Ashhab, N. Tabet and S. Kais, *Phys. Chem. Chem. Phys.*, 2016, **18**, 5219–5231; M. E. Madjet, G. R. Berdiyorov, F. El-Mellouhi, F. H. Alharbi, A. V. Akimov and Sabre Kais, Cation Effect on Hot Carrier Cooling in Halide Perovskite Materials, *J. Phys. Chem. Lett.*, 2017, **8**, 4439–4445.

49 A. Filippetti, A. Mattoni, C. Caddeo, M. I. Saba and P. Delugas, *Phys. Chem. Chem. Phys.*, 2016, **18**, 15352–15362.

50 S. D. Stranks, G. E. Eperon, G. Grancini, C. Menelaou, M. J. P. Alcocer, T. Leijtens, L. M. Herz, A. Petrozza and H. J. Snaith, *Science*, 2013, **342**, 341–344.

51 J. V. Passarelli, D. J. Fairfield, N. A. Sather, M. P. Hendricks, H. Sai, C. L. Stern and S. I. Stupp, *J. Am. Chem. Soc.*, 2018, **140**(23), 7313–7323.